# Nitric oxide generation by microwave capillary discharges under thermal control at atmospheric pressure

V. A. Sterie, Y. Zhao and G. D. Stancu*

Laboratoire EM2C, CNRS, CentraleSupélec, Université Paris-Saclay, Gif-sur-Yvette, France

Nitric oxide (NO) was generated inside capillary microwave discharges of 1-mm diameter, operating at 2.4 ÷ 2.5 GHz in mixtures of argon and air at atmospheric pressure. Time-resolved Mid-IR Quantum Cascade Laser Absorption Spectroscopy (QCLAS) was employed to measure the absolute density of NO molecules in *ex situ* conditions. The capillary post-discharge was coupled into a 50-cm White multi-pass cell where the laser was scanned over the ro-vibrational transition R (6.5), $v(0 \rightarrow 1)$, in the NO electronic ground state $X_{1/2}$ at 1900.076 cm$^{-1}$. It was found that NO density can be tuned over three orders of magnitude by varying the gas mixture and the discharge power. Enhancing the heat flux through the capillary has significantly extended the operating range of the discharge, increased the NO density and flowrate by almost one order of magnitude, and consequently reduced the energy cost. Molar fractions of NO up to 3,000 ppm ($7.1 \times 10^{16}$ cm$^{-3}$) with flowrates up to 7.2 sccm for discharge powers below 100 W have been obtained. Using a thermally controlled configuration, the energy cost of NO was found to be comparable to other efficient plasma sources at atmospheric pressure.

## 1 Introduction

Among the key reactive species generated by plasmas, nitric oxide has received a particular attention. Numerous investigations were focused on its reduction as it is often regarded as an environmental pollutant released from combustion systems [1, 2]. Known to play a key role in the regulation of biological processes, studies have also been conducted for wound healing and sterilization applications [3–5]. Furthermore, its plasma generation efficiency was investigated for medical use and for fertilizer production [6–8]. Currently, the fixation of atmospheric nitrogen by nitric oxide plasma synthesis is considered as a complementary approach to the Haber-Bosch process, which is known to have a global ecological impact [9].

Till now various atmospheric pressure non-thermal plasma sources generated in air or in gas mixtures of air with argon or helium were investigated for the NO production. This includes jets driven by kHz or MHz EM excitations, DBDs, glows, sparks, arcs, nanosecond and microwave discharges, in which nitric oxides were detected by FTIR, gas analyzers, mass spectrometry, optical emission spectroscopy, laser induced fluorescence, tunable diode laser absorption spectroscopy, quantum cascade laser absorption spectroscopy and cavity-enhanced absorption spectroscopy [7, 8, 10–17].
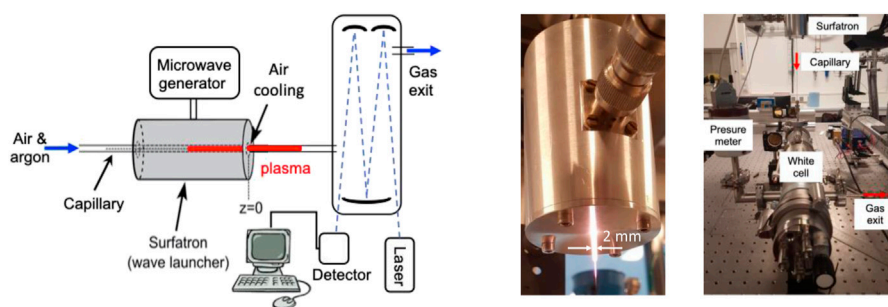
**FIGURE 1**
Experimental scheme including surfatron launcher and laser absorption system (left). Photo of the capillary microwave plasma (center). Picture of the White multi-pass cell connected to the capillary and the surfatron launcher (right).

Regarding microwave (mw) discharges, especially those sustained by surface waves inside dielectric tubes have proven to be very appealing for plasma applications. This is due to the electrodeless configuration (no plasma contamination), great flexibility and stability in operation conditions [18]. Recently, mw surface discharges within capillary diameters in the range of 1 mm–100 μm were efficiently generated by surfatron or stripline launchers. These capillary discharge sources are particularly attractive because they can produce high power density plasmas (up to 0.1 MW cm$^{-3}$) for low power inputs (tens of W) in gas mixtures ranging from mbar to atmospheric pressures [19–22]. A noteworthy feature is the slight power required to sustain plasmas that can be as low as 1 W. Studies in dry air at intermediate pressures have shown large radical productions (e.g., ~ 3% NO molar fraction, ~ 70% dissociation of $O_2$) and high vibrational excitations (e.g., $T_{vib}$ ~ 10,000 K), opening up prospects for applications also at atmospheric pressure [21, 23]. This type of plasma source has been adopted in the present research.

Here, the nitric oxide production potential was investigated in a 1 mm mw capillary discharge generated using a surfatron launcher at atmospheric pressure in air/argon gas mixtures. Time-resolved Mid-IR quantum cascade laser absorption spectroscopy (QCLAS) was employed to measure the absolute densities and production rates of NO molecules in the discharge exhaust. For this, the Mid-IR QCLAS was tuned over the ro-vibrational absorption line of NO [$X_{1/2}$, (0,1) R6.5] centered at 1900.076 cm$^{-1}$. The NO density, flowrate and energy cost were evaluated for different discharge parameters. An airflow cooling system has been designed to significantly enhance the heat transfer through the capillary. A study of the generation of NO under thermal control was also carried out.

The article is organized as follows. In Section 2, the experimental set-up for plasma generation and infrared laser absorption is detailed. In Section 3, the QCLAS principle and the time-resolved absorbance assessment are specified. Results and discussions are given in Section 4. This includes the study of the plasma working range, the thermal control analysis, the plasma parametric studies for NO generation and the literature comparison presenting diagnostic methods, atmospheric plasma sources and the related nitric oxide density, flowrate and energy cost. The conclusions of these investigations are presented in Section 5.
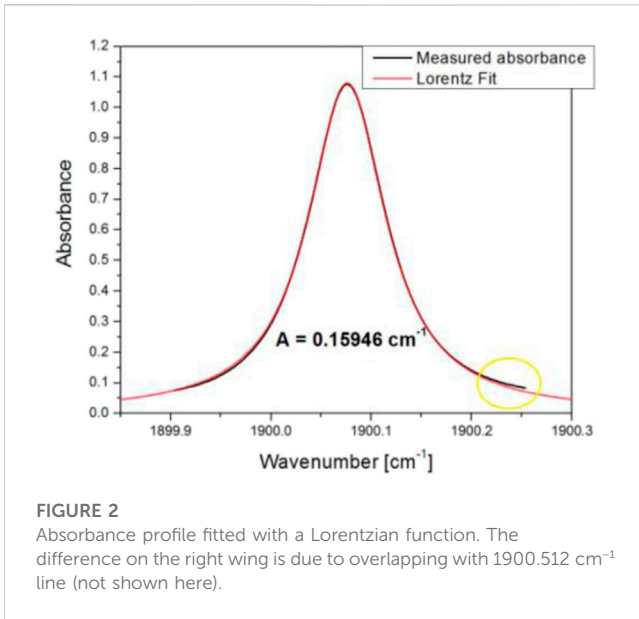
# 2 Experiment

## 2.1 Microwave capillary plasmas

The plasma source used for present investigations is similar to the configuration employed in Ref. [21]. The cw-microwave micro-plasmas were produced using a surfatron launcher inside a fused silica capillary (0.5 and 1 mm, inner and outer radii) in mixtures of argon and dry air. The capillary outlet was connected to a 50-cm length White multi-pass cell of 4 L volume in which a constant pressure of 1 atm was maintained. The total flowrate was changed in the range of 0.1–12 Nl/min, with the air/argon molar ratio from 1% to 40%. Power was supplied to the surfatron by a microwave generator (Sairem GMS200WSM56) working in the frequency domain 2.4 ÷ 2.5 GHz and with adjustable power in the range 1 ÷ 200 W. The microwaves were transmitted via a 1.5 m coaxial cable of 50 Ω impedance. At the end of the cable, a bidirectional coupler, MECA Electronics, 722N-30-3.100, was connected to the mw launcher. The coupler had an attenuation of 30(±1.2) dB on each measurement channel. Two powermeters, Minicircuits PWR-6GHS, were placed on each measurement channel. They operate in the range of −30 dB m to 20 dB m, with a typical uncertainty of ±0.15 dB m and a maximum uncertainty ±0.3 dB m for the power range used in current experiments. Figure 1 (left) shows a schematic representation of the experimental set-up. The capillary is centered axially and passes through the surfatron launcher. A plasma a few cm long is created inside the capillary. For some experiments, an airflow at room temperature with velocity of 10 ÷ 15 m/s was applied to the external surface of the capillary, to enhance the heat transfer from plasma to the external environment. For a capillary length of a few cm, the plasma can also be sustained outside the capillary. As shown in Figure 1 (center) a jet-like configuration can be realized.

## 2.2 Laser absorption set-up

Here is a brif description of the absorption set-up. More details can be found in Ref. [17]. The schematics of the QCLAS setup, which include the laser, the detector and a White multi-pass cell is shown in Figure 1 (left). An image of the White multi-pass cell connected by

FIGURE 2
Absorbance profile fitted with a Lorentzian function. The difference on the right wing is due to overlapping with 1900.512 cm$^{-1}$ line (not shown here).



FIGURE 3
Absorbance profiles recorded during about 13 min for a discharge power of 70 W, total flow rate of 800 Nml/min and air/argon ratio of 4%.

capillary to the surfatron launcher is presented in Figure 1 (right). The laser chip (Alpes Laser) was thermoelectrically cooled and driven by a Q-MACS system from Neoplas Control. The spectral resolution of the QCLAS system was $6 \times 10^{-3}$ cm$^{-1}$, the spectral scan was about 0.4 cm$^{-1}$ centered at 1900.076 cm$^{-1}$. Temporal resolutions down to 5 ms could be achieved. The output laser beam was collimated by a 90° off-axis gold-coated parabolic mirror with a focal point of 25.4 mm. The laser beam was then split into two parts using a calcium fluoride (CaF$_2$) beam splitter. The first part was used as a reference channel, in which a germanium etalon and a gas reference cell were employed for spectral calibration. For the second part, namely, the measurement channel, a couple of planar mirrors followed by a spherical mirror (150-cm focal) guided and focused the laser beam on the center of the White cell. After four passes, which represents an absorption length of 2 m, the laser beam was then focused on a Mid-IR photodetector (TE-PVI). The White multipass cell was coupled to the exhaust of the capillary plasma and an extraction pump. The length of the capillary was about 50 cm. A pressure meter (MKS PR4000B) was used to monitor the pressure inside the White cell. Argon and air mass flowrates were controlled using two Bronkhorst flowmeters.

# 3 QCLAS principle and time-resolved absorbance assessment

When passing through a uniform absorbing medium, the decay of monochromatic laser radiation is given by the Beer-Lambert's law:

$$I(\nu) = I_0(\nu) \exp(-k(\nu)L) \qquad (1)$$

where $I(\nu)$ is the transmitted beam intensity at a frequency $\nu$, $I_0(\nu)$ is the incident laser intensity, $L$ is the absorption length, and $k(\nu)$ is the absorption coefficient.
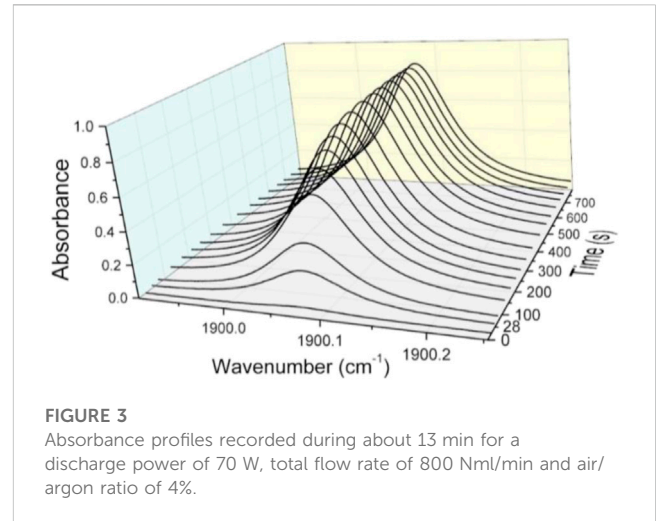
For a single ro-vibrational transition, the absorption coefficient can be expressed as a function of the temperature dependent line strength $S(T)$, the normalized line-shape function $f(\nu - \nu_0)$ and the total species density $N$:

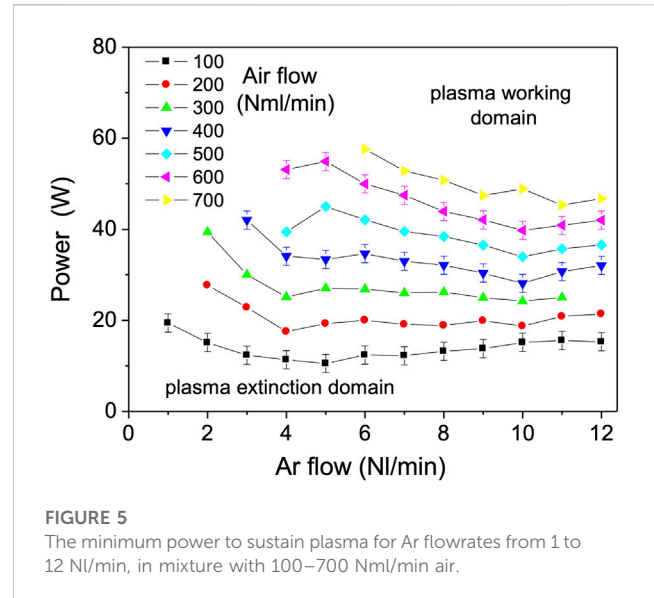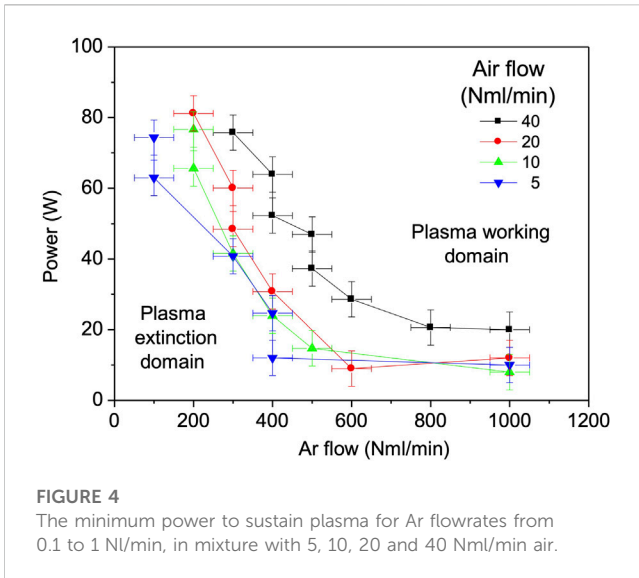$$k(\nu) = S(T)f(\nu - \nu_0)N = \frac{1}{L}\ln\left(\frac{I_0}{I}(\nu)\right) \qquad (2)$$

where $\nu_0$ is the transition resonance frequency. The species density can be determined using Eq. 3, where $S(T)$ is taken for NO from HITRAN data base [24]:

$$N = \frac{\int_\nu \nu \ln\left(\frac{I_0}{I}\right) d\nu}{S(T)L}. \qquad (3)$$

Due to collisional broadening that dominates the NO absorption line profile at atmospheric pressure, only a single absorption line centered at 1900.076 cm$^{-1}$ is observed over a spectral scan of 0.4 cm$^{-1}$. The line strength at 296 K for this spectrally unresolved absorption is $1.22 \times 10^{-19}$ cm [17].

The temperature of the exhaust gases that filled the White multipass cell was ambient temperature (i.e., 296 K). This was monitored using a thermocouple which was inserted inside the cell. In a continuous flow regime, the post-discharge gas cooled to room temperature due to the exposure to a large cell volume (4 L) of stainless-steel walls. Compared to direct absorption measurements in plasma, the use of the White cell here increases the measurement sensitivity by about three orders of magnitude.

At the beginning of each series of measurements, the laser intensity function of wavelength was recorded without plasma. This corresponds to the reference intensity $I_0(\nu)$ without NO presence. The transmitted intensity $I(\nu)$ was recorded in presence of plasma using the same integration time. By measuring these functions and based on Eq. 3, the NO density was then determined. Figure 2 shows a sample of NO absorbance spectrally resolved, $\ln[I_0(\nu)/I(\nu)]$, fitted with a Lorentzian function. The fit is generally very good. A slight difference is noted on the right wing. The measured absorbance is dimly larger than the fit function. As observed in [17], this is explained by the contribution of the nearest absorption line centered at 1900.512 cm$^{-1}$, which is

FIGURE 4
The minimum power to sustain plasma for Ar flowrates from
0.1 to 1 Nl/min, in mixture with 5, 10, 20 and 40 Nml/min air.



FIGURE 5
The minimum power to sustain plasma for Ar flowrates from 1 to
12 Nl/min, in mixture with 100−700 Nml/min air.

broadened by collisions at atmospheric pressure. However, this contribution remains negligible for the evaluation of the absorbance aria, which extends outside the spectral window as shown by the Lorentzian fit.

For all measurements presented here, the laser intensity function of wavelength was recorder with or without plasma. Each spectrum was registered at a frequency of 200 Hz. To increase the signal to noise ratio, an integration time of 20 s was considered. This corresponds to 4,000 averaged spectra. In Figure 3, a typical time evolution of NO absorbance is plotted. The spectra are recorded in *ex situ* conditions, a few tens of cm from the discharge which ignites at the zero time reference.

# 4 Experimental data analysis and comparison

## 4.1 Plasma domain and thermal control

Prior to the NO density measurements by the QCLAS technique, the working domain of the plasma was investigated for various flowrates, air/argon molar fractions and input powers. The length of plasma observed outside the surfatron was typically between 1 and 6.5 cm, for input powers of 10 and 80 W, respectively. The total plasma length is about a factor two longer. Approximately the same discharge volume is covered by the surfatron launcher and it is optically inaccessible [19]. The plasma volume was observed to diminish significantly when air was added in the percentage range. Injecting 1% of air in argon reduces the plasma length by almost a factor two, whereas for 10% air, the plasma length decreases to a few mm. Consequently, the plasma power per unit volume increases up to more than an order of magnitude. Under conditions of high-power density, the plasma gas temperature can exceed the capillary melting point. This significantly limits the discharge working domain if no external cooling is provided.

In Figure 4, the plasma working domain was determined for various input powers, Ar and airflow rates. The air molar fraction in

the mixture, computed by volume flowrates $\phi_{air}/(\phi_{Ar} + \phi_{air})$, varied between 0.5% and 11.7%. The curves plotted for airflow of 5, 10, 20 and 40 Nml/min show the minimum power to sustain the plasma. The regions above and below represent the plasma working and extinction domains, respectively. The minimum power to maintain plasmas inside the capillary was found to be about 10 W, which corresponds to the lowest molar fraction of air (~1%). Note that maximum power in these experiments was set to 85 W to avoid capillary damage. This happens especially during prolonged exposures to plasma containing a large percentage of air.

In Figure 5, the minimum power to sustain plasma inside the capillary was investigated for gas flows up to about one order of magnitude higher (12 Nl/min). The gas residence time in plasma is proportionally reduced. This adjustment is expected to decrease the plasma gas temperature and therefore expand the working range to higher air/argon fractions and powers. The last statement can be understood if one inspects the energy balance of an elementary fluid slab of length $dx$ in steady state given by,

$$\dot{m}cpdT_f = d\Phi, \qquad (4)$$

where $\dot{m}$ is the mass flowrate (Kg/s), $cp$, is the heat capacity (J/kg/K), $dT_f$, is the fluid mean temperature differential at $x + dx$ and $x$, and $d\Phi$ is the power (W) supplied or removed from the fluid. According to Eq. 4, for the same given power $d\Phi$, the fluid temperature differential is expected to be lower at higher flows.

Here too, powers down to 10 W were sufficient to maintain the plasma at the lowest air molar fractions (~1%). As before, the minimum power increases systematically when enhancing the air/argon molar fractions. Although the total flow could be increased up to 12.7 Nl/min, the air molar fractions in the mixture could not exceed 13% in these experiments. The power was kept even lower (below 60 W) to avoid capillary thermal damage.

Although the plasma gas temperature is expected to be lower, for the flow rates above 1.5 Nl/min, which corresponds to the Reynolds number of $Re_D \geq 2,300$, the flow regime becomes

turbulent. This is the flow regime expected for data in Figure 5. The heat transfer coefficient, $h$ (W/m$^2$/K), between the plasma and the capillary is then largely increased. Some estimates of $h$ coefficient can be made using a simple approach analysis. For an incompressible argon fluid in steady state and developed laminar regime with constant heat flux as the boundary condition, the Nusselt number reads,

$$Nu_D = \frac{h\,D}{\lambda} = 4.36, \tag{5}$$

where $D$ is the capillary internal diameter and $\lambda$ is the argon thermal conductivity. In case of the developed turbulent regime, the Nusselt number can be computed by,

$$Nu_D = \frac{h\,D}{\lambda} = 0.023 Re_D^{4/5} Pr^{0.3}, \tag{6}$$

where $Pr$ is the Prandtl number for argon, $Re_D = v\,\rho\,D/\mu$, $v$, $\rho$ and $\mu$ are argon fluid velocity, density and dynamic viscosity, respectively [25]. Using Eq. 6, an argon flow of 12 Nl/min at capillary exit conditions, will give $Nu_D = 155$. Consequently, although the plasma gas temperature is decreased due to higher mass flowrates, the heat transfer coefficient can be increased by a factor significantly higher than ten, for the same coupled power. Thus, the capillary temperature will approach the plasma gas temperature because the thermal resistance associated to conducto-convective phenomenon will be drastically reduced in the later case. This explains why the capillary plasma could only operate at relatively lower powers under the high flow conditions of Figure 5.

Higher powers and air/argon molar fractions are expected to contribute to efficient nitric oxide generation. However, in present experiments exceeding 85 and 60 W in Figures 4, 5, respectively for high air fractions and times longer than a few minutes resulted in partial damage or melting the capillary. To avoid this issue, reducing the heat flux generated by plasma or capillary cooling can be employed. Pulsing the microwave power can reduce the heat flux because less average power is then delivered to the plasma. As shown in [26], the inter-pulse cooling is very beneficial for NO production. Here we have applied an air-cooling flow to reduce capillary and plasma temperatures by enhancing the thermal flux through the capillary.

To determine the characteristics of the external airflow necessary to significantly alter the heat flux through the capillary, a thermal resistance model for heat transfer in steady state regime was analyzed. Since the radial temperature gradient is much larger than the axial gradient ($dT/dr >> dT/dx$), the longitudinal heat transfer inside the capillary can be neglected. Between the plasma, which is the heat source at temperature, $T_{plasma}$, and the external environment (air and laboratory walls), which is the heat sink at $T_{sink}$, the heat power, $d\Phi$, through a capillary slab of length $dx$, is limited by the total thermal resistance, $R_{th}$ which is given by [27],

$$d\Phi = \frac{T_{plasma} - T_{sink}}{R_{th}}. \tag{7}$$

According to Eq. 7, a significant change in heat power through the capillary can be attained by substantially varying the total

thermal resistance. The thermal resistance circuit for heat transfer from plasma to the external environment is shown below.
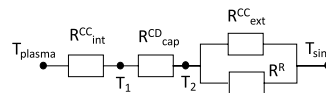


From the plasma to the internal capillary surface at temperature $T_1$, the heat is transferred by forced conducto-convection, with the corresponding resistance, $R_{int}^{CC}$. In the radial direction, the transfer to the external capillary surface at $T_2$ takes place by thermal conduction, with the corresponding resistance, $R_{cap}^{CD}$. The outer surface is then cooled by thermal radiation exchanges with the laboratory walls at temperature $T_{sink}$, the corresponding resistance, $R^R$, and by the external air at temperature $T_{sink}$, which is either natural convection or forced convection. The corresponding conducto-convective resistance $R_{ext}^{CC}$ can be significantly modified when the convection regime changes. As shown in [22], the capillary can be considered here as an opaque body for the thermal radiation domain. Also note that the thermal radiation flux at inner capillary surface is negligible. This is because the temperature is relatively uniform over longer lengths compared to the capillary radius.
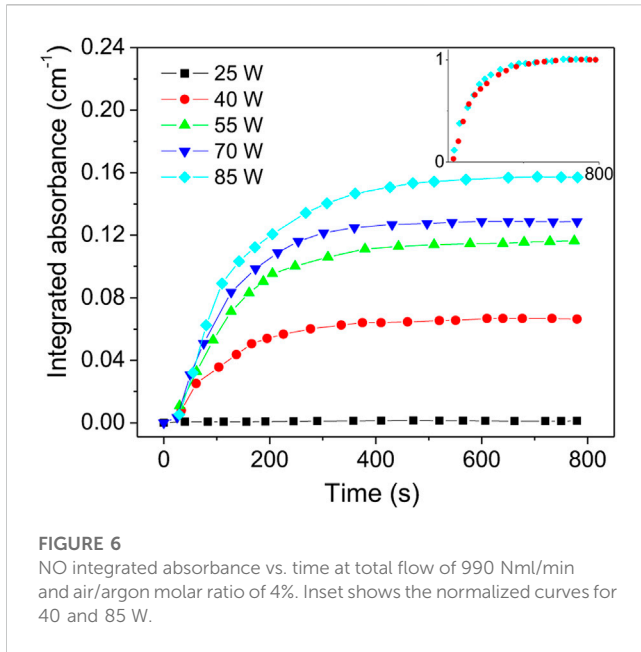
The thermal resistances mentioned above are determined by,

$$R_{cap}^{CD} = \frac{ln\,\frac{R_{ext}}{R_{int}}}{2\pi\lambda_{cap}dx}, R_{int}^{CC} = \frac{1}{h^{cc}\,2\pi R_{int}dx}, R_{ext}^{CC} = \frac{1}{h^{cc}\,2\pi R_{ext}dx}, \text{and}$$

$$R^R = \frac{1}{h^R\,2\pi R_{ext}dx}. \tag{8}$$

Where the conducto-convective transfers coefficients, $h^{cc} = Nu_D \lambda_{fluid}/D$ ($\lambda_{fluid}$, the thermal conductivity of argon or air, $D$, the internal or external capillary diameters) are obtained based on correlations for natural convection, internal and external forced convection. $\lambda_{cap}$ is the thermal conductivity of the capillary, $R_{ext}$ and $R_{int}$ are capillary external and internal radii. The radiative heat transfer coefficient, $h^R$ is evaluated by $h^R = 4\varepsilon\sigma T_m^3$, when $\Delta T \ll T$, with $\varepsilon$ capillary emissivity, the Stefan-Boltzmann constant, $\sigma = 5.67 \times 10^{-8} \frac{W}{m^2 K^4}$, and $T_m$ is the average of the temperatures of the outer surface of the capillary and the lab walls.

Thermal resistances change significantly for conditions under present investigations. In the following, a range of values was determined for each resistance component using Eq. 8. The conductive capillary resistance is estimated as $dxR_{cap}^{CD} \in (0.079 \div 0.046)$ Km/W, assuming temperatures of 300 and 1,000 K. The thermal conductivity temperature dependence was taken from [28]. For the argon flow in the forced internal convection, the corresponding resistance is in the range $dxR_{int}^{CC} \in (1.7 \div 4.1)$ Km/W for the same temperatures, assuming a laminar regime and with the argon thermal conductivity taken from [29]. The analogous resistance for the capillary external cooling by natural convection, is estimated as $dxR_{ext}^{CC} \in (6 \div 11)$ Km/W, for the external capillary surface between 700 K and ambient air. The Nusselt number is determined here for a horizontal cylinder of diameter $D$, following the procedure from [22] with the correlation,

$$Nu_D = \left\{ 0.6 + \frac{0.387 Ra_D^{1/6}}{[1 + 0.721\,Pr^{-9/16}]^{8/27}} \right\}^2 \tag{9}$$

**FIGURE 6**
NO integrated absorbance vs. time at total flow of 990 Nml/min and air/argon molar ratio of 4%. Inset shows the normalized curves for 40 and 85 W.



**FIGURE 7**
NO steady state density and flowrate function of power computed for conditions of data from Figure 6.

from [30], where $Ra_D$ is the Rayleigh number. It is estimated that forced convection due to air cooling applied perpendicular to the capillary at speed of $10 \div 15$ m/s reduces up to a factor ten the corresponding resistance, namely, $dxR_{ext}^{CC} \in (0.55 \div 0.65)$ Km/W. The Nusselt number is determined here using the correlation,

$$Nu_D = 0.3 + \frac{0.62 Re_D^{1/2} Pr^{1/3}}{[1 + 0.543/Pr^{2/3}]^{1/4}} [1 + 3.92 \times 10^{-4} Re_D^{5/8}]^{4/5} \quad (10)$$

from [31]. Because the thermal radiation that occurs in parallel with the external conducto-convective phenomenon is not linearizable ($\Delta T \sim T$), an equivalent radiative coefficient can be determined by, $h^R = \varepsilon\sigma(T_{cap}^4 - T_{wall}^4)/(T_{cap} - T_{wall})$. For the capillary external surface lower than 700 K and walls at the ambient temperature, the corresponding radiative resistance is found in the range $dxR^R \in (6 \div 32)$ Km/W. Note that the capillary emissivity is wavelength dependent in the Mid-IR region. This aspect was taken into account using the approach discussed in Ref. [22].

Based on the resistance circuit, by changing the air-cooling thermal resistance from natural to forced convection, it ultimately reduces the total resistance on average by a factor 2.5. Therefore, applying an airflow with velocities of $10 \div 15$ m/s on the capillary surface should increase the heat flux approximately the same factor. Consequently, the temperatures $T_{plasma}$, $T_1$ and $T_2$ will be reduced. As reported in [32], the plasma gas temperature can be reduced up to about a factor two when such external air cooling is applied. Significant changes in pressure and electron density were also observed.

Appling this procedure allowed the plasma working domain to extend for air/argon ratios up to 40% (air molar fraction of 28.6%) and for powers up to 84 W. As discussed in the following subsections, this triggers a significant increase in NO density and an important reduction in energy cost per molecule.
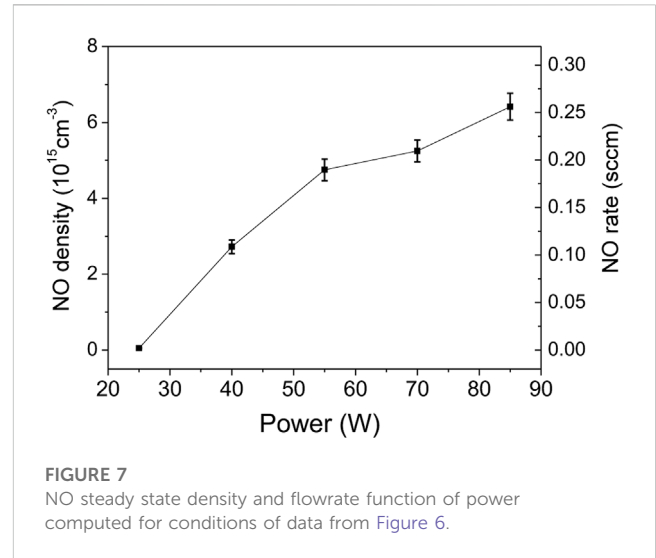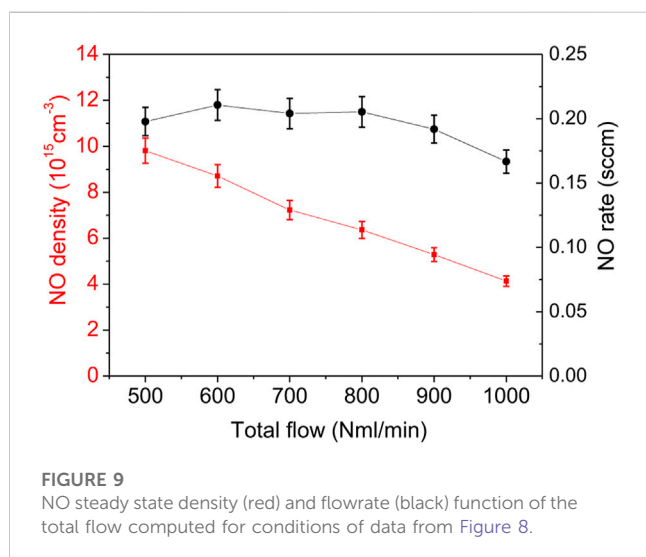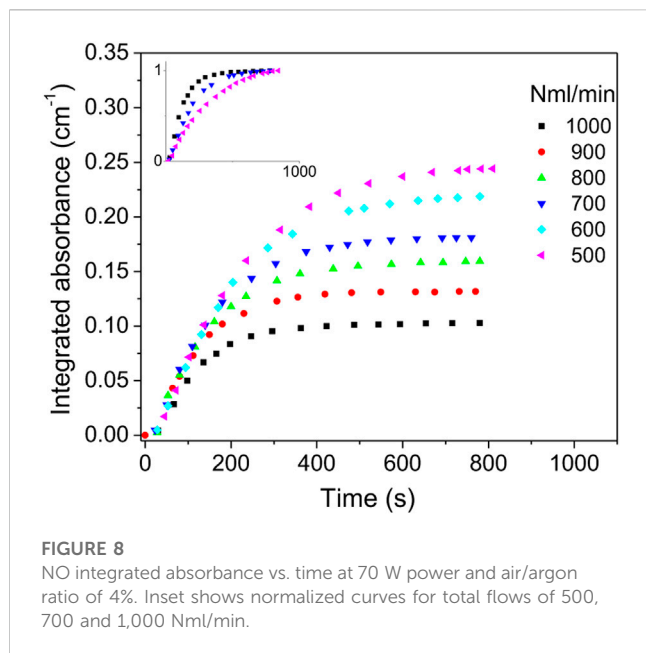
## 4.2 NO parametric studies

The NO generation was investigated under variations in discharge power, gas flowrate, air/argon molar fraction and using an external capillary air cooling system. As shown in Figure 3, the NO absorbance increases with time and reaches a steady state regime at about 500 s. To ensure steady state conditions, measurements were performed for extended durations for each plasma parameter study.

The first parametric study included the variation of the discharge power while keeping constant the total flowrate (990 Nml/min) and the air/argon molar fraction (4%). For each change in the input power, measurements were taken over a period of about 13 min. In Figure 6 the integrated NO absorbance function of time for powers from 25 to 85 W are presented. It is observed that NO integrated absorbance is close to zero at 25 W and increases monotonically with the discharge power. In the inset of Figure 6, the 40 and 85 W curves were normalized. However, all normalized curves exhibit identical behavior, namely, the time derivative is independent of the plasma power. Using the data from Figure 6, the absorbance values obtained at the steady state were used to compute NO absolute densities. This data are presented in Figure 7. The error bars are mainly determined from the data statistics of two series of measurements. A temperature variation of ± 2 K and an absorption length error of ± 5 cm were considered. A maximum NO density of $6.5 \times 10^{15}$ cm$^{-3}$ (260 ppm) and corresponding rate of 0.26 sccm are obtained at 85 W. The NO production flowrate in sccm units is computed as, $\Phi_{NO} = \Phi \times [NO]/N_{total}$, where $\Phi$ is the total flow and $N_{total}$, is the total density calculated to be $2.48 \times 10^{19}$ cm$^{-3}$. The increase of NO density with the discharge power can be explained by the increase of the plasma gas temperature. Note that NO density in the air composition at equilibrium peaks around 3,500–4,000 K [33], which is much higher than the upper temperature for capillary continuous use (~1,400°C). Increasing the power is expected to promote further the nitric oxide. However, running the discharge at higher powers resulted in capillary thermal damage.

In the second experiment, the total gas flow varied between 500 and 1,000 Nml/min for a constant air/argon molar ratio of 4%

**FIGURE 8**
NO integrated absorbance vs. time at 70 W power and air/argon ratio of 4%. Inset shows normalized curves for total flows of 500, 700 and 1,000 Nml/min.



**FIGURE 10**
NO density and flowrate function of air/argon molar ratio at total flow of 440 Nml/min and power of 70 W.



**FIGURE 9**
NO steady state density (red) and flowrate (black) function of the total flow computed for conditions of data from Figure 8.

and an input power of 70 W. In Figure 8, the integrated absorbance is plotted versus time for various flows. NO absorbance reaches steady state after about 300 s for 1,000 Nml/min, while for 500 Nml/min steady state is reached after 700 s. In the inset of Figure 8, the curves of 500, 700 and 1,000 Nml/min were normalized. It is observed that the slopes at origin are increasing with the total flowrate. This different behavior compared to data in Figure 6 can be explained by the species convection phenomenon. The flow convection speed in the cell can be evaluated by $v_m = \phi_m / \rho_m A$, where $\phi_m$ is the mixture mass flow rate (i.e., 14.7 μg/s at 500 Nml/min and 4% air), $\rho_m$ is the mixture mass density (i.e., 1.61 kg/m³) at the temperature and pressure conditions of the cell (1 atm, 296 K), and $A$ is the aria of the cell cross-section (78.5 cm²). For a 0.5 m length cell, this gives flow velocities of about 1.2 and 2.3 mm/s, which corresponds to
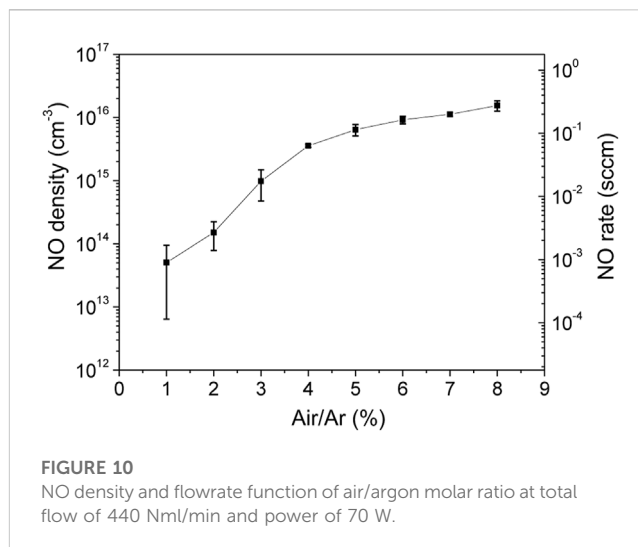
characteristic convection times of about 420 s and 220 s for 500 and 1,000 Nml/min, respectively. Thus, the NO generated by plasma fills the 4-L cell in a duration of the order of these characteristic times.

Nitric oxide is expected to be converted to the more stable nitric dioxide ($NO_2$) by reaction, $NO + NO + O_2 \rightarrow NO_2 + NO_2$. The characteristic time of this reaction for the White cell conditions can be determined by, $\tau_{1/2} = 1/k[O_2][NO]$, where $k = 1.93 \times 10^{-38} cm^6/s$ [34]. Its value is estimated here on the order of a few hours. As the White cell is placed several tens of cm downstream of the plasma, no other long-lived species are expected to change the NO density. Thus, the absorbance time dependency shown in Figure 8 is determined by fluid transport.

To calculate the steady state NO density, the same procedure as above was followed. The NO density and flowrate results are shown in Figure 9. The NO density of up to $10^{16}$ cm$^{-3}$ (400 ppm) is obtained at the lowest flow rate. The density increases by about a factor 2.3 when the flowrate is reduced by a factor 2. The increase in NO flow rate is relatively less important, i.e., from 0.17 sccm to 0.2 sccm, i.e., below 20%.

In the next set of experiments, the air/argon molar ratio was varied, while keeping power and total gas flowrate constant at 70 W and 440 Nml/min, respectively. In Figure 10, the steady state density was measured for air molar ratio in the range 1%–8%. These investigations were done at the lowest gas flowrate for which plasma can be maintained with a wide range of air/argon molar fractions. Error bars are determined primarily by data statistics from two set of experiments. The NO density increases about three orders of magnitude when rising the air/argon fraction from 1% to 8%. The NO maximum density is found $1.5 \times 10^{16}$ cm$^{-3}$ (660 ppm) which corresponds to a maximum NO flow rate of 0.27 sccm.

These sets of experiments clearly indicate that higher powers and air/argon fractions lead to higher NO densities and production rates. The following experiments were carried out under the conditions shown in Figure 5. The NO density function of Ar flowrate from 1 to 6 Nl/min measured for a constant air/argon molar ratio of 5% and for 30, 35, 40 and 50 W is shown in Figure 11. As before, the highest density (~$10^{16}$ cm$^{-3}$) is measured at lowest
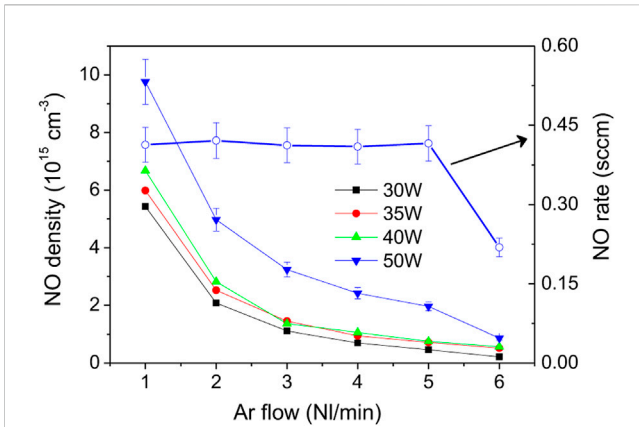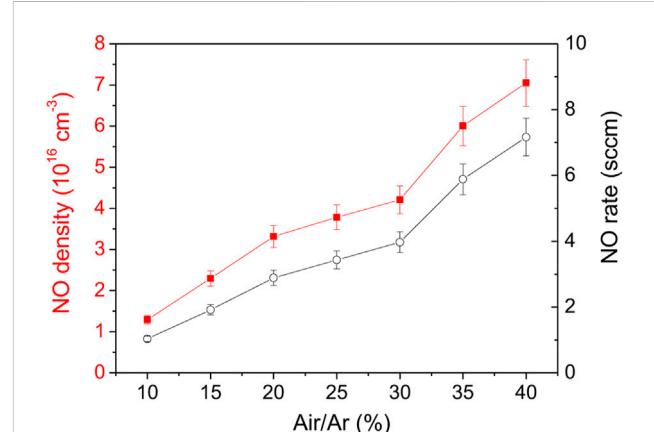
**FIGURE 11**
NO density function of Ar flowrate for air/argon molar ratio of 5%. For 50 W the NO flowrate values are plotted in blue circles.
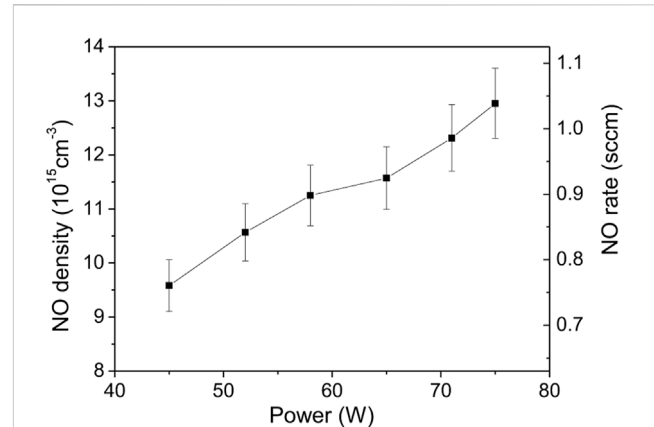


**FIGURE 13**
NO density function of power for air/Ar molar ratio of 10% and total flowrate of 2 Nl/min.
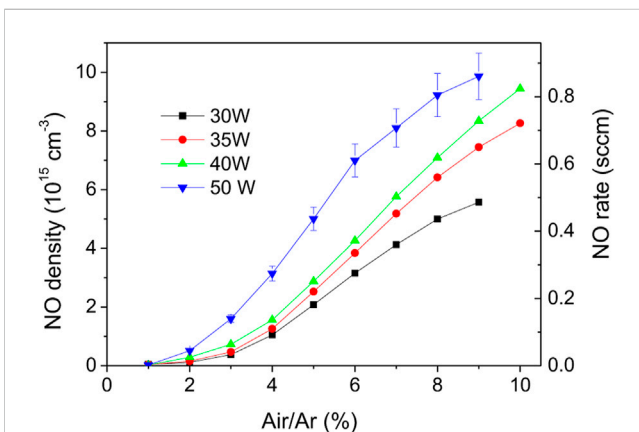


**FIGURE 12**
NO density and flowrate function of air/argon molar ratio for 2 Nl/min Ar flowrate.



**FIGURE 14**
NO density function of air/Ar molar ratio for 1.8 Nl/min Ar flowrate and 84 W.

flow and at highest power. The maximum NO flowrate is obtained at 50 W and is relatively higher than previous experiments (i.e., 0.41 sccm compared to 0.27 sccm). Flowrate values at 50 W shows a significant decrease at 6 Nl/min. This is probably attributed to the enhancement of the turbulent regime, which alters the thermal behavior of the capillary plasma, as discussed in the previous subsection. In Figure 12, the NO density and flowrate are plotted against the air/argon molar ratio for a constant Ar flow of 2 Nl/min. Although the maximum NO density is limited to about $10^{16}$ cm$^{-3}$, the NO flowrate was increased up to a factor two when the air/argon ratio is 10% (i.e., 0.41 sccm versus 0.83 sccm).

The last set of experiments were performed using the air-cooling system applied to the outer surface of the capillary. The goal was to maximize the plasma power and the air/argon molar fraction while avoiding capillary thermal damage. In Figure 13, NO density was measured for powers up to 75 W for an air/Ar molar ratio of 10% and a total flow of 2 Nl/min. Here the maximum NO density and flowrate were increased by about 30% compared to previous studies.

Note that the highest NO values were obtained in Figure 14, where for a power of 84 W, the air/argon ratio was varied between 10% and 40%. The maximum NO density measured in steady state reaches $7.1 \times 10^{16}$ cm$^{-3}$ (about 3,000 ppm) for a NO flowrate of 7.2 sccm. Compared to the uncooled capillary, this corresponds to an increase of almost an order of magnitude. Thus, the enhancement of the heat transfer through the capillary turns out to be another essential parameter to produce NO.

## 4.3 Literature comparison: NO density, flowrate, energy cost

There are many studies on nitric oxide generated by discharges at atmospheric pressure. Reviews on NO plasma sources, detection methods and production related to medical or nitrogen fixation applications can be found, for example, in Refs. [7, 35, 36]. However, data on NO flowrate and energy costs are fewer and comparison of

**TABLE 1** Representative discharge sources, detection methods and NO generation characteristics at atmospheric pressure conditions.

| Discharge | Method | Location | Molar fraction (ppm) or density | Flow (sccm) | Energy cost (keV/molec) | References |
|---|---|---|---|---|---|---|
| Streamer | LIF | *in situ* | 25 | 0.08 | 1.2 (NOx: 4000 GJ/tN) | Roth [38] |
| DC streamer corona | LIF | *in situ* | 200 | | | Kanazawa [39] |
| DBD | FTIR | 2 cm | 2,000 | | | Pei [40] |
| Ns streamer | LIF | 5 mm | $10^{16}$ cm$^{-3}$ | | 3.5 (20 W) | Yagi [41] |
| kINPen-APPJ | QCLAS | *ex situ* | 8 | | | Pipa [42] |
| RF-APPJ | LIF | *in situ* | $1.5 \times 10^{15}$ cm$^{-3}$ | <0.032 | >3.2 (7.4 W) | van Gessel [43] |
| Pulse-APPJ | LIL | *in situ* | $2.5 \times 10^{14}$ cm$^{-3}$ | | | Yonemori [44] |
| kINPen-APPJ | LIF | 0 ÷ 7 mm | $2.5 \times 10^{14}$ cm$^{-3}$ | | | Iseni [37] |
| μ-APPJ | QCLAS | *ex situ* | 3.22 | 0.0045 | 4.6 (1.5 W) | Douat [11] |
| Transient spark | Gas analyzer | *ex situ* | 400 | 0.68 | 0.123 (6 W) | Janda [45] |
| NRP discharge | QCLAS | *in situ* | $2 \times 10^{15}$ cm$^{-3}$ | | | Simeni [17] |
| Spark discharge | LIF | 3 mm | 10,000 | 5 | 0.080 | Britun [16] |
| Pulsed arc | Gas analyzer | *ex situ* | 540 | 1.08 | 0.129 (10 W) | Namihira [46] |
| Pulsed arc | FTIR | *ex situ* | 1,060 | | | Sakai [47] |
| Pulsed arc | Gas analyzer | *ex situ* | | | 0.016 | Wang [48] |
| Propelor arc | FTIR | *ex situ* | 3,000 | 9 | 0.059 (38 W) | Pei [40] |
| Plasmatron | Gas analyzer | *ex situ* | 3,200 | 20 | 0.035 | Korolev [49] |
| Microwave | MS | *ex situ* | 25,000 | | 0.056 | Taras [50] |
| Microwave | Gas analyzer | *ex situ* | 202 | 1.2 | 0.79 | Kim [51] |
| μ-Microwave | Electrochem | 25 mm | 2,750 | 0.58 | | Kühn [52] |
| Microwave | LIF | 0 ÷ 15 mm | $1.4 \times 10^{15}$ cm$^{-3}$ | | | van Gessel [53] |
| Microwave capillary | QCLAS | *ex situ* | 3,000 | 7.2 | 0.16 (84 W) | Present work |

literature results requires special attention. For instance, the power considered for the evaluation of the energy cost is generally that transferred to plasma and not the overall consumption of the power supply. The energy cost can vary by an order of magnitude depending on the power component taken into account [16]. Measurements in the effluent at different distances from plasmas, where chemical equilibrium is not reached can also yield an order of magnitude changes in NO density [37].

To compare current data with previous studies, energy efficiency was evaluated. The energy cost for NO generation by plasma can be expressed in units of eV/molecule and determined by, $\eta = P/\Phi_{NO}$, where $P$ is the discharge power (eV/s) and $\phi_{NO}$ is the NO flowrate (molecule/s). The conversion is performed using 1 W = 6.241 × $10^{18}$ eV/s and 1 sccm (1Nml/min) = 4.478 × $10^{17}$ molecule/s, respectively.

For present experiments, the data in Figure 14 (84 W and 7.2 sccm) give the best NO production efficiency, namely, a cost of 160 eV/molecule. This corresponds to NO density of 7.1 × $10^{16}$ cm$^{-3}$ and a molar fraction of 3,000 ppm. Note that this energy cost is much lower than the data recorded without the external cooling device. Figure 11 and Figure 13 give about 0.6 keV/molecule and 3.5 keV/molecule, respectively.

In Table 1, some representative data for NO generation by atmospheric pressure plasma sources and detection methods together with present results are shown. When data was available, NO flowrates were computed based on NO molar fractions and total flowrates. The energy costs were converted in eV/molecule units or evaluated using powers provided in publications. Compared to atmospheric pressure plasma jets (APPJ) and dielectric barrier discharges (DBD), the present mw capillary discharges demonstrate to be significantly superior. The NO density and flowrate are shown appreciably larger and the energy cost per molecule is found lower by about one order of magnitude. The mw capillary discharge show to be comparable with other microwave discharges and plasma sources such as pulsed or gliding arcs and sparks. However, with energy cost below 100 eV/molecule a few experiments are shown to perform better. Among them we can cite the near equilibrium microwave plasma of Taras et al. [50], which produces 2.5% NO for 6 J/Nml air, an equivalent of 56 eV/molecule. Plasma sources such as plasmatron or pulsed arcs performed even better with energy costs down to 16 and 35 eV/molecule [48, 49].

Recently Britun et al. [16] and Verloessem et al. [26] using a spark discharge and a pulsed plasma jet announced record energy

costs for NO (or $NO_x$) production with values on the order of 4 eV/molecule. The high efficiency for NO generation was attributed to the non-thermal Zeldovich mechanism: 1) $N_2(X,v) + O \leftrightarrow NO + N$, 2) $O_2(X,v) + N \leftrightarrow NO + O$ involving vibrationally excited nitrogen and oxygen molecule [7, 9]. Efficient cooling by acting on gas flow or pulsing the discharge reduces reverse reactions, vibrational-vibrational and vibrational-translational relaxation processes [26, 54]. However, as mentioned in [16] this low cost is based on the power absorbed by plasma. When the DC power applied to discharge generator is taken into account, the lowest energy cost is 80 eV/molecule instead of 4 eV/molecule. It shout be noted that this remains well above the energy cost of nitrogen fixation by Haber-Bosch route, currently assessed at approximately 5 eV/molecule [7].

Concerning the present capillary microwave studies, we should mention that the NO energy cost was determined using *ex situ* conditions which is not always the case for experiments in Table 1. The density of NO was measured at tens of cm from the discharge zone and at room temperature conditions, therefore in a frozen chemical regime. Moreover, as shown in the recent paper of Coquery et al. [22] the actual coupled power in microwave capillary plasmas could be up to an order of magnitude less than the value given by the usual balance of incident and reflected powers. This method was retained here and is commonly employed in the literature. Thus, if only the power coupled to the plasma is considered, the energy cost can be significantly lower than the present value.

## 5 Conclusion

In this work nitric oxide was generated using microwave capillary discharges in air/argon mixtures under atmospheric pressure conditions. The Mid-IR quantum cascade laser absorption spectroscopy was used to measure time resolved NO absolute densities in *ex situ* conditions.

Parametric studies have shown that the highest NO production is obtained for the highest power and air/argon molar ratio. Mw capillary discharges have proven to be a robust source of nitric oxide with densities and flowrates tuned over three orders of magnitude. It was found that increasing the total mass flowrate in plasma significantly reduces the energy cost of NO. However, discharge operation was limited to lower input powers. The enhancement of the heat transfer in the turbulent regime explains the capillary thermal degradation.

By controlling the heat transfer through the capillary with an airflow cooling system, the discharge working domain was significantly extended. Nitric oxide density and flowrate increased near one order of magnitude, reaching a maximum of $\times 7.1 \ 10^{16} \ cm^{-3}$ (3,000 ppm) and 7.2 sccm, for an input power of 84 W. Consequently, the energy cost per NO molecule was reduced by

about an order of magnitude, to a minimum value of 160 eV/molecule.

Microwave capillary discharges have demonstrated about one order of magnitude higher NO efficiency than APPJ and DBD discharges and energy costs comparable to the top efficient plasma sources. Although the energy cost is still a factor higher than the best in the literature, the results are very encouraging for further developments. Recently, it was found that a large mw power contributes to the heating of the mw launcher. Thus, if the energy cost is evaluated using the absorbed plasma power, the value reported here will be considerably lower. Moreover, by further enhancing the heat transfer through the capillary (e.g., employing a cooling fluid with a better exchange coefficient or a thinner capillary) or by pulsing the discharge, efficiency improvements are expected.

## Data availability statement

The raw data supporting the conclusion of this article are available from the corresponding author on reasonable request.

## Author contributions

VS and YZ have substantially contributed to the data acquisition. GS has contributed to the conception, data analysis and interpretation and drafting the work.

## Funding

## Conflict of interest

The authors declare that the research was conducted in the absence of any commercial or financial relationships that could be construed as a potential conflict of interest.

## Publisher's note

All claims expressed in this article are solely those of the authors and do not necessarily represent those of their affiliated organizations, or those of the publisher, the editors and the reviewers. Any product that may be evaluated in this article, or claim that may be made by its manufacturer, is not guaranteed or endorsed by the publisher.

## References

1. Bowman CT. Control of combustion-generated nitrogen oxide emissions: Technology driven by regulation. *Symp Combust* (1992) 24:859–78.

2. Ju Y, Sun W. Plasma assisted combustion: Dynamics and chemistry. *Prog Energ Combust. Sci.* (2015) 48:21–83.

3. Liebmann J, Scherer J, Bibinov N, Rajasekaran P, Kovacs R, Gesche R, et al. Biological effects of nitric oxide generated by an atmospheric pressure gas-plasma on human skin cells. *Nitric Oxide - Biol Chem* (2011) 24:8–16. doi:10.1016/j.niox.2010.09.005

4. Kong MG, Kroesen G, Morfill G, Nosenko T, Shimizu T, Van Dijk J, et al. Plasma medicine: An introductory review. *New J Phys* (2009) 11:115012. doi:10.1088/1367-2630/11/11/115012

5. Kuwahara T, Kuroki T, Yoshida K, Saeki N, Okubo M. Development of sterilization device using air nonthermal plasma jet induced by atmospheric pressure corona discharge. *Thin Solid Films* (2012) 523:2–5. –5. doi:10.1016/j.tsf.2012.05.064

6. Qian L, Wenlu Z, Hong W, Juan D, Xinli T, Linlin W, et al. Design and study of nitric oxide portable producing device using continuous discharging arc plasma reaction keeping low energy efficiency for viral pneumonia emergency therapy. *PLoS One* (2020) 15:e0237604. doi:10.1371/journal.pone.0237604

7. Patil BS, Wang Q, Hessel V, Lang J. Plasma N2-fixation: 1900–2014. *Catal Today* (2015) 256:49–66. doi:10.1016/j.cattod.2015.05.005

8. Pei X, Gidon D, Graves DB. Specific energy cost for nitrogen fixation as NOxusing DC glow discharge in air. *J Phys D Appl Phys* (2020) 53:044002. doi:10.1088/1361-6463/ab5095

9. Cherkasov N, Ibhadon AO, Fitzpatrick P. A review of the existing and alternative methods for greener nitrogen fixation. *Chem Eng Process* (2015) 90:24–33. doi:10.1016/j.cep.2015.02.004

10. Pipa AV, Bindemann T, Weltmann K. *Measurements of NO generated by atmospheric pressure plasma jet (APPJ) by absorption and emission spectroscopy 1614–7* (2007).

11. Douat C, Hübner S, Engeln R, Benedikt J. Production of nitric/nitrous oxide by an atmospheric pressure plasma jet. *Plasma Sourc Sci. Technol.* (2016) 25:025027. doi:10.1088/0963-0252/25/2/025027

12. Stancu GD, Simeni Simeni M, Laux CO. *Study of nitric oxide and carbon monoxide production in plasma assisted combustion by QCLAS 21st International Symposium on Plasma Chemistry (Cairns, Australia)* (2013).

13. Hong YJ, Lim J, Choi JS, Weltmann KD, Choi EH, Measurement of nitrogen dioxide and nitric oxide densities by using CEAS (cavity-enhanced absorption spectroscopy) in nonthermal atmospheric pressure air plasma *Plasma Process Polym* (2020) 18 2000168. doi:10.1002/ppap.202000168

14. Iséni S, Reuter S, Weltmann KD. NO2 dynamics of an Ar/Air plasma jet investigated by *in situ* quantum cascade laser spectroscopy at atmospheric pressure. *J Phys D Appl Phys* (2014) 47:075203. doi:10.1088/0022-3727/47/7/075203

15. Foltynowicz A, Masłowski P, Ban T, Adler F, Cossel KC, Briles TC, et al. Optical frequency comb spectroscopy *Faraday Discuss* (2011) 150 23–31.

16. Britun N, Gamaleev V, Hori M. Evidence of near-the-limit energy cost NO formation in atmospheric spark discharge. *Plasma Sourc Sci. Technol.* (2021) 30: 08LT02. doi:10.1088/1361-6595/ac12bf

17. Simeni Simeni M, Laux CO, Stancu GD. High-spatial resolution measurements of NO density and temperature by Mid-IR QCLAS in open-air confined plasmas. *J Phys D Appl Phys* (2017) 50:274004. doi:10.1088/1361-6463/aa72ca

18. Ferreira CM, Moisan M. *Microwave discharges fundamentals and applications (nato ASI series B: Physics.* Springer Science+Business Media New York (1993).

19. Dap S, Leroy O, Andrieu J, Boisse-Laporte C, Leprince P, Stancu GD, et al. Hydrodynamic and thermal effects of continuous microwave-sustained plasma in capillary tubes. *Plasma Sourc Sci. Technol.* (2015) 24:065007. doi:10.1088/0963-0252/24/6/065007

20. Debord B, Alves LL, Gérôme F, Jamier R, Leroy O, Boisse-Laporte C, et al. Microwave-driven plasmas in hollow-core photonic crystal fibres. *Plasma Sourc Sci. Technol.* (2014) 23:015022. doi:10.1088/0963-0252/23/1/015022

21. Stancu GD, Leroy O, Coche P, Gadonna K, Guerra V, Minea T, et al. Microwave air plasmas in capillaries at low pressure II. Experimental investigation. *J Phys D Appl Phys* (2016) 49:435202. doi:10.1088/0022-3727/49/43/435202

22. Coquery F, Leroy O, Minea T, Stancu G. Plasma power balance: Methodology and investigations of microwave capillary discharges. *Plasma Sourc Sci. Technol.* (2022) 5: 055003. doi:10.1088/1361-6595/ac6691

23. P Coche VG, Alves LL. Microwave air plasmas in capillaries at low pressure I. Self-consistent modeling. *J Phys D Appl Phys* (2016) 49:235207. doi:10.1088/0022-3727/49/23/235207

24. Rothman LS, Barbe A, Chris Benner D, Brown L, Camy-Peyret C, Carleer M, et al. The HITRAN molecular spectroscopic database: Edition of 2000 including updates through 2001. *J Quant Spectrosc Radiat Transf* (2003) 82:5–44. doi:10.1016/s0022-4073(03)00146-8

25. Dittus FW, Boelter LMK. Heat transfer in automobile radiators of the tubular type. *Int Commun Heat Mass Transf* (1985) 12:3–22. doi:10.1016/0735-1933(85)90003-x

26. Vervloessem E, Gorbanev Y, Nikiforov A, De Geyter N, Bogaerts A. Sustainable NOx production from air in pulsed plasma: Elucidating the chemistry behind the low energy consumption. *Green Chem* (2022) 24:916–29. doi:10.1039/d1gc02762j

27. Whitaker S. *Fundamental principles of heat transfer*. Pergamon Press INC (1977).

28. Combis P, Cormont P, Gallais L, Hebert D, Robin L, Rullier JL. Evaluation of the fused silica thermal conductivity by comparing infrared thermometry measurements with two-dimensional simulations. *Appl Phys Lett* (2012) 101:211908. doi:10.1063/1.4764904

29. Chen SH, Saxena SC. Thermal conductivity of argon in the temperature range 350 to 2500 k. *Mol Phys* (1975) 29:455–66. doi:10.1080/00268977500100391

30. Churchill SW, Chu HHS. Correlating equations for laminar and turbulent free convection from a horizontal cylinder. *Int J Heat Mass Transf* (1975) 18:1049–53. doi:10.1016/0017-9310(75)90222-7

31. Churchill SW, Bernstein M. A correlating equation for forced convection from gases and liquids to a circular cylinder in crossflow. *J Heat Transfer* (1977) 99:300–6. doi:10.1115/1.3450685

32. Coquery F, Spectroscopic characterization and thermal coupling of microwave plasmas in capillaries (2021) CentraléSupélec, Université Paris-Saclay. PhD Thesis.

33. Gilmore FR. *Equilibrium composition and thermodynamic properties of air to 24,000°* Santa Monica. K U.S. Air Force (1955). *RM-1543* 1–75.

34. Atkinson R, Baulch DL, Cox RA, Crowley JN, Hampson RF, Hynes RG, et al. Evaluated kinetic and photochemical data for atmospheric chemistry: Volume I - gas phase reactions of $O_x$, $HO_x$, $NO_x$ and $SO_x$ species. *Atmos Chem Phys* (2004) 4:1461.

35. Ono R. Optical diagnostics of reactive species in atmospheric-pressure nonthermal plasma. *J Phys D Appl Phys* (2016) 49:083001. doi:10.1088/0022-3727/49/8/083001

36. Malik MA. Nitric oxide production by high voltage electrical discharges for medical uses: A review. *Plasma Chem Plasma Process* (2016) 36:737–66. doi:10.1007/s11090-016-9698-1

37. Iseni S, Zhang S, Van Gessel AFH, Hofmann S, Van Ham BTJ, Reuter S, et al. Nitric oxide density distributions in the effluent of an RF argon APPJ: Effect of gas flow rate and substrate. *New J Phys* (2014) 16:123011. doi:10.1088/1367-2630/16/12/123011

38. Roth GJ, Gundersen MA. Laser-induced fluorescence images of NO distribution after needle-plane pulsed negative corona discharge. *IEEE Trans Plasma Sci* (1999) 27: 28–9. doi:10.1109/27.763011

39. Kanazawa S, Ito T, Shuto Y, Ohkubo T, Nomoto Y, Mizeraczyk J. *Two-dimensional distribution of ground-state NO density by LIF technique in DC needle-to-plate 37 1663* (2001).

40. Pei X, Gidon D, Yang YJ, Xiong Z, Graves DB. Reducing energy cost of NO production in air plasmas. *Chem Eng J* (2019) 362:217–28. doi:10.1016/j.cej.2019.01.011

41. Yagi I, Shirakawa Y, Hirakata K, Akiyama T, Yonemori S, Mizuno K, et al. Measurement of OH, O, and NO densities and their correlations with mouse melanoma cell death rate treated by a nanosecond pulsed streamer discharge. *J Phys D Appl Phys* (2015) 48:424006. doi:10.1088/0022-3727/48/42/424006

42. Pipa AV, Bindemann T, Foest R, Kindel E, Röpcke J, Weltmann KD. Absolute production rate measurements of nitric oxide by an atmospheric pressure plasma jet (APPJ). *J Phys D Appl Phys* (2008) 41:194011. doi:10.1088/0022-3727/41/19/194011

43. van Gessel AFH, Alards KMJ, Bruggeman PJ. NO production in an RF plasma jet at atmospheric pressure. *J Phys D Appl Phys* (2013) 46:265202. doi:10.1088/0022-3727/46/26/265202

44. Yonemori S, Ono R. Effect of discharge polarity on the propagation of atmospheric-pressure helium plasma jets and the densities of OH, NO, and O radicals Effect of discharge polarity on the propagation of atmospheric-pressure helium plasma jets and the densities of OH. *N Biointerphases* (2015) 10:029514.

45. Janda M, Martisovits V, Hensel K, Machala Z. Generation of antimicrobial NO x by atmospheric air transient spark discharge. *Plasma Chem Plasma Process* (2016) 36: 767–81. doi:10.1007/s11090-016-9694-5

46. Namihira T, Katsuki S, Hackam R, Akiyama H, Okamoto K. Production of nitric oxide using a pulsed arc discharge. *IEEE Trans Plasma Sci* (2002) 30:1993–8. doi:10.1109/tps.2002.807502

47. Sakai S, Matsuda M, Wang D, Namihira T, Akiyama H, Okamoto K, et al. Nitric oxide generator based on pulsed arc discharge. *ACTA Phys Pol A* (2009) 115:1104–6. doi:10.12693/aphyspola.115.1104

48. Wang Y, Desilva AW, Goldenbaum GC, Dickerson RR. Nitric oxide production by simulated lightning: Dependence on current energy and pressure. *J Geophys Res* (1998) 103:19149–59. doi:10.1029/98jd01356

49. Korolev YD, Frants OB, Landl NV, Suslov AI. Low-current plasmatron as a source of nitrogen oxide molecules. *IEEE Trans Plasma Sci* (2012) 40:2837–42. doi:10.1109/tps.2012.2201755

50. Taras P, Dusek V, Vyskocil P. Study of the NO synthesis in a microwave plasma at atmospheric pressure. *Acta Phys Slov* (1985) 35:112.

51. Kim T, Song S, Kim J, Iwasaki R. Formation of NO x from air and N 2/O 2 mixtures using a nonthermal microwave plasma system. *Jpn J Appl Phys* (2010) 49: 126201. doi:10.1143/jjap.49.126201

52. Kühn S, Bibinov N, Gesche R, Awakowicz P. Non-thermal atmospheric pressure HF plasma source: Generation of nitric oxide and ozone for bio-medical applications. *Plasma Sourc Sci. Technol.* (2010) 19:015013. doi:10.1088/0963-0252/19/1/015013

53. van Gessel AFH, Hrycak B, Jasiński M, Mizeraczyk J, van der Mullen JJAM, Bruggeman PJ. Temperature and NO density measurements by LIF and OES on an atmospheric pressure plasma jet. *J Phys D Appl Phys* (2013) 46:095201. doi:10.1088/0022-3727/46/9/095201

54. Vervloessem E, Aghaei M, Jardali F, Hafezkhiabani N, Bogaerts A. Plasma-based $N_2$ fixation into $NO_x$: Insights from modeling toward optimum yields and energy costs in a gliding arc plasmatron. *ACS Sustain Chem Eng* (2020) 8:9711–20. doi:10.1021/acssuschemeng.0c01815